

## Achieving Novel States through Shock-Wave Loading of Pre-Compressed Samples

Raymond Jeanloz,<sup>1</sup> Peter M. Celliers,<sup>2</sup> Gilbert W. Collins,<sup>2</sup> John H. Eggert,<sup>2</sup> Kanani K. M. Lee,<sup>3</sup>  
Paul Loubeyre<sup>4</sup>

<sup>1</sup>Department of Earth and Planetary Science and of Astronomy, University of California, Berkeley, CA 94720; <sup>2</sup>Lawrence Livermore National Laboratory, Livermore, CA; <sup>3</sup>New Mexico State University, Las Cruces, NM; <sup>4</sup>CEA, Bruyeres, France

**Materials can be experimentally characterized to TPa pressures by sending a laser-induced shock wave through a sample that is pre-compressed inside a diamond-anvil cell. This combination of static- and dynamic-compression methods provides access to the 10-100 (why not .01 to 1 Gbar etc?) TPa (0.1-1 Gbar) pressure range that is relevant to planetary science, to testing first-principles theories of condensed matter, and to experimentally studying a new regime of chemical bonding.**

In nature, and specifically when considering planets, high pressures are clearly evident in two contexts: the conditions occurring deep inside large planetary bodies, and the transient stresses caused by hypervelocity impact among planetary materials. In both cases, typical peak pressures are much larger than the crushing strength of minerals (up to about ~1-10 GPa, depending on strain rate, pressure and temperature), so can be evaluated by disregarding strength and treating the rock or ice as a fluid. Ignoring the effects of compression, the central (hydrostatic) pressure of a planet is therefore expected to scale roughly as the square of the planet's average density ( $\rho_{planet}$ ) and radius ( $R_{planet}$ ):

$$P_{center} \sim 7 \text{ TPa } (\rho_{planet}/\rho_{Jupiter})^2 (R_{planet}/R_{Jupiter})^2 \quad (1)$$

Here the scaling factor is matched to Jupiter-like planets, and the effects of compression and of differentiation (segregation of dense materials toward the center of a planet) act to increase the central pressure for larger or denser planets relative to (1). Consequently, peak pressures in the 1-10 TPa range exist inside large planets, with Earth's central pressure being 0.37 TPa and "super-giant" planets being expected to have central pressures in the 10-100 TPa range.

In addition to static considerations, impacts, which is a key process associated with growth of planets and the initial heating that drives the geological evolution of planets, is also expected to generate TPa pressures. Impedance-matching considerations described below can be combined with Kepler's third law to deduce that peak impact pressures for planetary objects orbiting a star of mass  $M_{star}$  at an orbital distance  $R_{orbit}$  are of the order

$$P_{impact} \approx 1 \text{ TPa } (M_{star}/M_{Sun}) (\rho_{planet}/5.5 \text{ g cm}^{-3}) (R_{orbit}/1 \text{ AU})^{-1} \quad (2)$$

Scaling here is to the mass of the Sun, and the average density and orbit of Earth, the latter being in astronomical units (1 AU = 1.496 x 10<sup>11</sup> m); also, the characteristic impact velocity ( $u_0$ ) is taken as the average orbital velocity according to Kepler's law,  $u_0 = 2\pi R_{orbit}/T_{orbit}$  with  $T_{orbit}$  being the orbital period.

LLNL 9/6/06 3:59 PM

Deleted: Similarly,

LLNL 9/6/06 3:59 PM

Deleted: i

LLNL 9/6/06 4:00 PM

Deleted: Thus, impact – the key process associated with growth of planets and the initial heating that drives the geological evolution of planets – is also expected to generate TPa pressures. .

While recognizing that materials have been characterized at such conditions through specialized experiments (e.g., shock-wave measurements to the 10-100 TPa range in the proximity of underground nuclear-explosion tests, and from impact of a foil driven by hohlraum-emitted x-rays) (1-3), laboratory experiments tend to achieve significantly lower pressures. As with planetary phenomena, both static (diamond-anvil cell) and dynamic (shock-wave) methods are available for studying macroscopic samples at high pressures, but these are normally limited to the 0.1-1 TPa range (4). Still, these pressures are of fundamental interest because the internal-energy change associated with compression to the 0.1 TPa (1 Mbar) level is roughly (5)

$$\Delta E \approx -P \Delta V \sim 10^5 \text{ J per mole of atoms} \quad (3)$$

with volume changes ( $\Delta V$ ) being approximately 20% of the 5 cm<sup>3</sup> typical molar volume of condensed matter (here we consider a mole of atoms, or gram-formula weight, which is 3.5, 5 and 6 cm<sup>3</sup> for diamond, MgO and water, respectively, at ambient conditions). The work of compression thus corresponds to typical bonding energies ( $\sim 1 \text{ eV} = 96 \text{ kJ per mole}$  characteristic of the outer, bonding electrons of atoms), meaning that the chemical bond is profoundly changed by pressures of 0.1 TPa. This expectation has been verified through numerous experiments showing that the chemical properties of matter are significantly altered under pressure: for instance, hydrogen, oxygen and the “noble gas” xenon transform from insulating, transparent fluids or crystals at zero pressure (and low temperature) to become metals by  $\sim 10^{11} \text{ Pa}$  (5, 6).

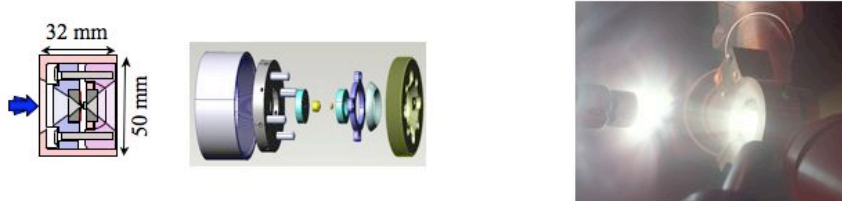


**Fig. 1.** Schematic of diamond-anvil cell (*left*), showing both a cross-section (blue arrow indicates direction of incoming, shock-wave generating laser beams) and a pulled-apart view, and photograph (*right*) of a diamond cell as a laser-induced shock is being generated during an experiment at the Omega laser facility (University of Rochester).

In the present article, we briefly describe laboratory techniques that have recently been developed for studying materials to the 10-100 TPa range of relevance to planetary science. In particular, as most planets now known are supergiants of several ( $\sim 1.5$ -8) Jupiter masses orbiting stars at distances of a fraction of 1 AU (7), (1)-(2) imply a strong motivation for characterizing materials up to the 100 TPa (1 Gbar) level. In order to reach such conditions, we combine static and dynamic techniques for compressing samples: specifically, propagating a shock wave through a sample that has been pre-compressed in a diamond-anvil cell (Fig. 1). By starting with a material that is already at high (static) pressures, one not only reaches much higher pressures upon shock compression, but also higher compressions than could be obtained by driving a shock directly into an uncompressed sample. Moreover, by varying the initial density (pressure) of the sample, one can tune the final pressure-density-temperature ( $P$ - $\rho$ - $T$ ) state that is achieved.

## Experimental Approach

Diamond-cell samples are necessarily small,  $\sim 100\text{-}500\text{ }\mu\text{m}$  diameter by  $5\text{-}50\text{ }\mu\text{m}$  thickness, as it is the small area of the diamond tip (culet) that allows high pressures to be achieved. Shock-compression of such small samples is not well suited to experiments involving mechanical impact, for example by a projectile launched from a light-gas gun (which currently sets the state of the art for high-quality shock-wave measurements, but involves sample dimensions of  $\sim \text{cm}$  diameter by mm thickness). Instead, a laser-generated shock-wave is better suited to the dimensions of the diamond cell, with a well-defined shock front of about  $200\text{-}500\text{ }\mu\text{m}$  diameter being readily achieved at presently available facilities.

Several laser beams are typically focused onto the outer surface of one of the diamond anvils, so as to generate an intense pulse of light that is absorbed at the diamond surface (a thin coating of an absorbing medium is generally deposited on that diamond surface). The outermost diamond is thereby vaporized, launching a high-amplitude pressure wave into the anvil due to a combination of the rapid thermal pressure generated in the diamond and linear-momentum balance (“rocket effect”) relative to the diamond vapor that expands outward, back toward the incoming laser beams. Such a high-amplitude wave has the property of being self-steepening for a material with a normal equation of state ( $\partial K_S/\partial P > 0$  for the adiabatic bulk modulus  $K_S$ ). As a result, a shock-front is created inside the anvil and propagates toward the sample (8, 9).

The sample itself is pre-compressed inside a metal gasket, either directly (e.g., if it is a fluid) or else within a pressure-transmitting fluid (Fig. 2). Current methods allow samples to be pre-compressed up to no more than  $\sim 1\text{-}10\text{ GPa}$ , because the diamond anvil from which the shock-front enters needs to be thin, no more than about  $100\text{-}400\text{ }\mu\text{m}$  thick (10, 11). This amounts to little more than a microscope-slide cover slip, albeit made of diamond. As discussed below, this limitation arises from the short duration of laser pulses available at present-day facilities.

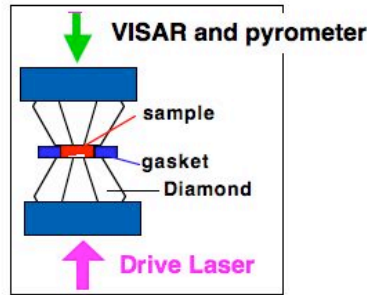


**Fig. 2.** Schematic cross-section of diamond anvils and sample, with the drive-laser that creates the shock wave entering from below (as described in the text, current laser systems require the anvil on the shock-entry side to be thin). The sample is indicated, along with a stepped shock-wave calibrant, and diagnostics described in the text (VISAR and pyrometry) record the dynamic compression of the sample through the second anvil.

Two types of calibrants are included in the gasket hole, along with the sample: one or more small ( $\sim 1\text{-}10\text{ }\mu\text{m}$ ) chips of ruby, and a shock-wave standard. The ruby is used to measure the pressure of the pre-compressed sample ( $P_1$ ), using the ruby-fluorescence method (12), from

which the density of the sample ( $\rho_1$ ) is determined prior to shock compression (the equation of state of the sample must therefore be known at the pressures of the pre-compression). The shock-wave standard typically consists of a metal plate, stepped so as to have at least two well-determined thicknesses. The metal must be a shock-wave standard, (i.e., well-determined relationship between shock and particle velocities,  $U_s$  and  $u_p$ ). Aluminum, platinum and tungsten are examples of shock-wave standards, and a measurement of the shock velocity (the shock-wave transit-times across the different, well-calibrated thicknesses of the standard) then yields the particle velocity of the shock-front entering into the sample (13).

Upon exiting the first diamond anvil, the shock front traverses the sample chamber (including both sample and calibrants) and then transits through the second (back) diamond anvil. At this point, there is no concern if the shock-wave decays, so the back anvil can be of typical thickness for high-pressure experiments ( $\sim 2.5$  mm); it serves as a window, containing and allowing the sample to be characterized during shock-compression. Both anvils as well as the sample (and calibrants) are normally vaporized during an experiment, although the cell that contains the anvils is re-useable. With shock velocities of order  $\sim 10$  km/s =  $10 \mu\text{m}/\text{ns}$ , the entire experiment is completed within a few nanoseconds.

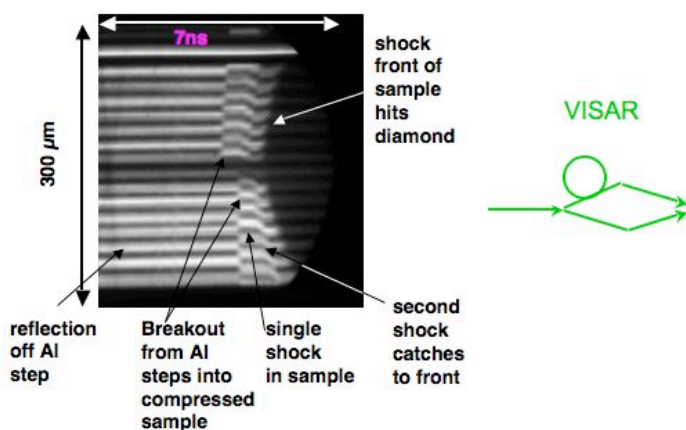


**Fig. 3.** VISAR record (*left*) from a laser-shock experiment through a pre-compressed sample (14), showing velocity fringes as a function of time (horizontal axis) obtained from an electronic streak camera imaging light reflected off the stepped-Al shock standard ( $\sim 300 \mu\text{m}$  width across the sample area). Schematically (*right*), VISAR operates by splitting the laser light reflected off a sample (including the stepped shock standard within the sample area) with a beam splitter, and recombining the two images at the detector after one of them has been sent through a delay line (e.g., a fiber-optic loop, indicated on the upper path). Thus, the detector records superimposed images that show the sample at two different time intervals; the resulting fringes indicate displacements (in multiples of a wavelength), so for a given delay-line time difference these represent velocities of the reflecting interfaces.

A set of forward- and backward-travelling stress waves (shock or rarefaction) is in general created at each interface between diamond, calibrant and sample, so a complete temporal record is needed of the various waves that traverse the sample. This is usually accomplished by velocity interferometry, VISAR (15), that provides a record of the shock and material (particle)

velocities inside the sample chamber (Fig. 3). If the initial thickness of the (pre-compressed) sample is known, a measurement of the shock-wave transit time determines the shock velocity.

The pressure ( $P_H$ ), density ( $\rho_H$ ) and internal energy change ( $E_H - E_1$ ) of the sample during shock compression is then determined by the Hugoniot relations that describe conservation of mass, linear momentum and energy ( $V = 1/\rho$  is specific volume) (8):

$$\rho_1 U_S = \rho_H (U_S - u_p) \quad (4)$$

$$P_H - P_1 = \rho_1 U_S u_p \quad (5)$$

$$E_H - E_1 = (1/2) (P_H + P_1) (V_1 - V_H) \quad (6)$$

Here, subscripts H and 1 indicate the shock-compressed (Hugoniot) state and the initial, unshocked (in the present case, statically pre-compressed) state, respectively;  $U_S$  is the velocity of the shock front (assumed to be steady), and  $u_p$  is the particle velocity to which the material is accelerated upon shock loading (without loss of generality, the material is taken as having  $u_p = 0$  prior to shock compression). These relations describe a one-dimensional compression such that, for unit cross-section,  $U_S$  and  $\rho_1 U_S$  define a volume and corresponding mass of unshocked material that is engulfed by the shock front in unit time. That mass is compressed to a volume  $U_S - u_p$  having a density  $\rho_H$ ; the volume change (per unit cross section and mass engulfed by the shock front in unit time) is thus given by  $-u_p$  in (4). The pressure change across the shock front is the force per unit cross section, or the mass  $\rho_1 U_S$  times the acceleration  $u_p$  in (5). Finally, (6) states that half the  $-P\Delta V$  compressional energy change is lost in accelerating the material to the velocity  $u_p$  on shock loading (the internal energy is expressed in  $\text{J/kg} = \text{m}^2 \text{s}^{-2}$  here).

It is empirically found that the shock-wave velocity scales linearly with particle velocity for a wide variety of materials over a moderate range of compressions (8, 13, 16, 17):

$$U_S = c + s u_p \quad (7)$$

Therefore, the Hugoniot pressure (5) scales as  $\sim u_p^2$  and the energy change (6) deposited into unit volume of the sample scales as  $\sim u_p^3$ . For a laser-produced shock wave, assuming the energy deposited into the sample is proportional to the laser intensity  $I$  at least for a moderate range of intensities, one consequently expects the shock pressure to scale roughly as

$$P \sim I^{2/3} \quad (8)$$

In reality, laser-induced shock pressures appear to rise less rapidly than (8), the exponent being closer to 0.6 than 0.7, no doubt due to inefficiencies in laser-target coupling that can become worse as  $I$  increases (18, 19) and to  $U_S$  ultimately increasing sub-linearly with  $u_p$  (deviations from (7) typically involve a negative contribution quadratic in  $u_p$  (e.g., 2), and the occurrence of phase transitions under shock compression likewise reduces  $U_S$  at a given  $u_p$ ).

Although reasonable for understanding the conditions achieved by laser-driven shock waves, (8) is inadequate for determining the properties – notably, the equation of state – of a sample at high pressures. Instead, one applies the fact that conservation of mass and momentum require that both the particle velocity and pressure be constant across each interface traversed by the shock wave(s) (8, 16). Measuring the shock velocity, hence pressure, density and particle

velocity in the stepped shock-wave standard (blue point in Fig. 4), determines the magnitude of the stress wave entering the sample itself. The material velocity and pressure of the sample and standard are brought to the common values  $u_p$  and  $P_H$  across the interface (red point in Fig. 4): the pressure in the standard decreases or increases, respectively, depending on whether it is less or more compressible than the sample (Fig. 4 illustrates the former case, with the pressure drop in the standard indicated by the curved blue arrow; in detail, a correction is made in order to account for the fact that the decompression follows an isentrope rather than the Hugoniot).

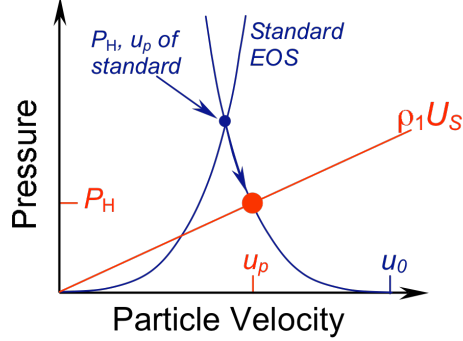


**Fig. 4.** Impedance matching solution for the Hugoniot pressure ( $P_H$ ) and particle velocity ( $u_p$ ) in the sample, as determined from the shock velocity  $U_S$  measured across the sample that by (5) defines the slope of the red line ( $P_1$  is ignored here). The intersection with the equation of state of the standard (blue curve), reflected about the pressure–particle velocity state achieved in the standard (blue point), defines the common state (red point) behind the forward- and backward-travelling waves in the sample and standard. In a mechanical-impact experiment,  $u_0$  would correspond to the impact velocity of the standard into the sample.

#### Conditions Achieved

In order to evaluate the conditions generated in laser-shock experiments on pre-compressed samples, we calculate the Hugoniot equation of state by way of the Mie–Grüneisen approach that takes the sample pressure (Hugoniot pressure  $P_H$  achieved on shock loading) as arising from two terms, compression along a reference path to the final volume ( $V$ ) plus thermal pressure at that (constant) volume (16, 17):

$$P_H(V) = P_S(V) + (\gamma/V) [E_H(V) - E_S(V)] \quad (9)$$

Here, the reference path is an isentrope, indicated by subscript  $S$ , and the Grüneisen parameter  $\gamma = V(\partial P/\partial E)_V$  depends on volume but is dimensionless and assumed not to depend on temperature (in fact, as described below, ionization causes  $\gamma$  to depend on temperature).

The internal energy along the isentrope,  $E_S(V)$ , is given by the isentropic equation of state  $P_S(V)$  because  $-(\partial E/\partial V)_S = P$ . We specifically use the Eulerian finite-strain formulation for the isentrope, motivated by the fact that the Cauchy stress (the trace of which gives the pressure) is intrinsically a function of Eulerian strain (20), and that the resulting equation of state is empirically found to successfully match experimental measurements involving both finite and infinitesimal compression (e.g., wave-velocity measurements) (17, 21). That is, the internal

energy change upon isentropic compression is assumed well-described by a Taylor expansion in the Eulerian finite-strain measure  $f = (1/2) [(V/V_0)^{-2/3} - 1]$  (defined positive on compression)

$$\Delta E_S = (9/2) V_0 K_{0S} f^2 [1 + (K_{0S}' - 4)f + \dots] \quad (10)$$

$K$  is the bulk modulus, subscript zero indicates zero-pressure conditions and prime is for differentiation as a function of pressure. The coefficients have been evaluated in (10) such that  $P_S$  and  $\Delta E_S$  both vanish as  $f$  goes to zero. The resulting  $P$ - $V$  equation of state (Birch–Murnaghan form) is

$$P_S = 3 K_{0S} f (1 + 2f)^{5/2} [1 + (3/2)(K_{0S}' - 4)f + \dots] \quad (11)$$

Combining (9) with (6) yields

$$P_H = \{P_S + (\gamma/V_H)[(P_1(V_1 - V_H)/2 + \int_{V_1}^{V_H} P_S dV)]\} \{1 - (\gamma/V_H)(V_1 - V_H)/2\}^{-1} \quad (12)$$

with  $P_1 = P_1(V_1)$  being the pre-compression pressure at volume  $V_1$ , and  $P_H = P_H(V_H)$  and  $P_S = P_S(V_H)$  are the Hugoniot and isentrope pressures at volume  $V_H$ . Here, we ignore the possibility of phase transformations in order to avoid complicating the discussion, but such transformations (e.g., solid–solid, or melting) can be taken into account if the equation of state and initial energy of the high pressure phase is known. Consequently, applying (10) and (11) to (12), the Hugoniot pressure normalized by the zero-pressure adiabatic bulk modulus is

$$\frac{P_H}{K_{0S}} = \{A + B + C\} \left\{ 1 - \frac{\gamma}{2} \left[ \left( \frac{1 + 2f_H}{1 + 2f_1} \right)^{3/2} - 1 \right] \right\}^{-1} \quad (13a)$$

$$A = 3 (1 + 2f_H)^{3/2} f_H \{1 + [2 + (3/2)(K_{0S}' - 4 - \gamma)]f_H + 3(K_{0S}' - 4)[1 - (\gamma/2)]f_H^2 + \dots\} \quad (13b)$$

$$B = 9 (\gamma/2) (1 + 2f_H)^{3/2} f_1^2 [1 + (K_{0S}' - 4)f_1 + \dots] \quad (13c)$$

$$C = 3 (\gamma/2) (1 + 2f_1)^{3/2} f_1 [(1 + 2f_H)^{3/2} - (1 + 2f_1)] [1 + (3/2)(K_{0S}' - 4)f_1 + \dots] \quad (13d)$$

Without pre-compression, the terms  $B$  and  $C$  vanish and the denominator in (13a) is simplified.

In order to focus on general scaling relations, rather than detailed calculations for specific materials, we assume  $K_{0S}' = 4$  (second-order or Birch equation of state),  $\gamma/V = \gamma_0/V_0 = \text{constant}$  and  $\gamma_0 = 1.5$  because these are typical values for condensed matter ( $K_{0S}' \approx 3$ -6 and  $\gamma_0 \approx 1$ -2 in most instances) (17). In addition, we treat the pre-compression as being isentropic rather than isothermal, ignoring the percent-level difference between the isotherm and isentrope pressure at volume  $V_1$ . The results show that Gbar (100 TPa) pressures are expected for materials compressed  $\sim 10$ - to  $20$ -fold for the Hugoniot and isentrope (or isotherm), respectively (Fig. 5). Detailed pressures would differ for different parameter values than those assumed here (larger values of  $\gamma$  increase the Hugoniot pressure at a given volume, and larger values of  $K_{0S}'$  increase both the adiabat and Hugoniot pressure at a given volume). Also, more terms may be needed in

the finite-strain expansions (10), (11) and (13) at high compressions; by the same token, a limitation of the linear  $U_S - u_p$  relation (7) is evident from the figure (it can be shown that the Hugoniot pressure becomes infinite for a compression  $\rho/\rho_0 = s/(s-1) = 5$  for the value of  $s$  used here (16)).

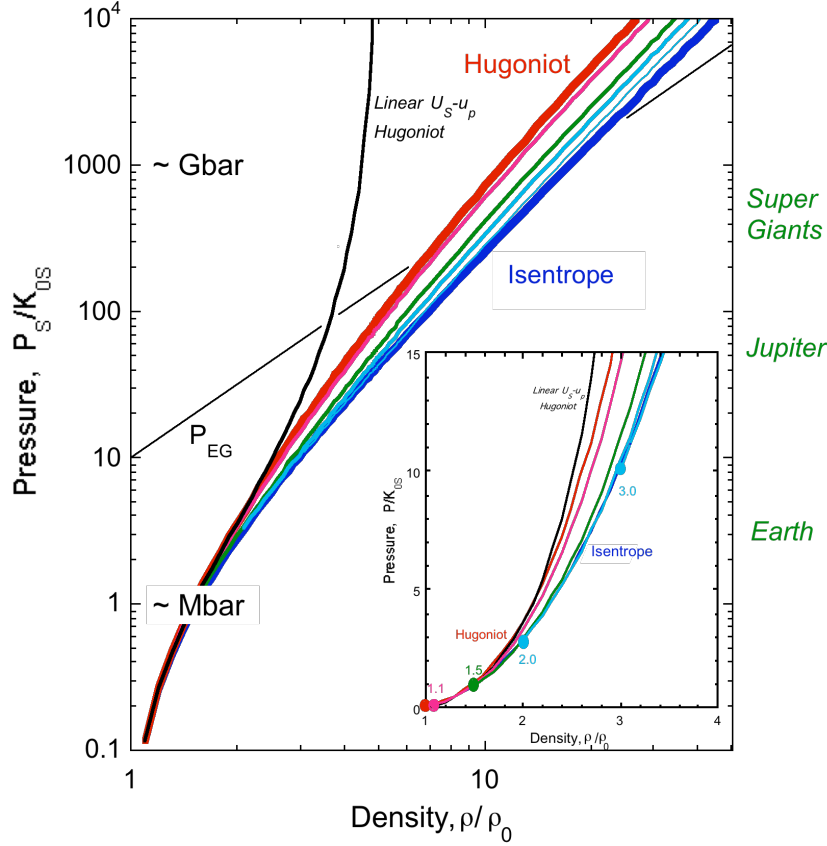


**Fig. 5.** Predicted pressure–density equations of state for condensed matter, due to isentropic compression (Inset: heavy dark blue curve), shock compression (Hugoniot: heavy red curve) and shock compression of samples pre-compressed to initial densities of  $\rho/\rho_0 = 1.1, 1.5, 2.0$  and  $3.0$  (unlabelled thin red, green, turquoise and blue curves: see Fig. 6) assuming  $K_{0s}' = 4$  and  $\gamma_0 = 1.5$ . Pressure and density are normalized to the zero-pressure bulk modulus and density, respectively, and the Mbar (100 GPa) and Gbar (100 TPa) pressure regimes are indicated based on a typical value of  $K_{0s} = 10^{11}$  Pa (corresponding central pressures for Earth, Jupiter and super-giant planets are indicated on the right). The Hugoniot for the linear  $U_S - u_p$  relation (7) and the density dependence of the electron–gas pressure,  $\bar{P}_{EG} \sim \rho^{5/3}$  (8) are shown by thin black and grey lines (because  $c$  in (7) is the zero-pressure bulk sound velocity,  $(K_{0s}/\rho_0)^{1/2}$ , its value is absorbed in the pressure normalization used here; in accord with  $K_{0s}' = 4$  for the finite-strain calculations, we set  $s = 5/4$  (17)). Conditions near zero pressure are shown on a linear plot (inset) to complement the log–log plot of the main figure.



The effect of pre-compression is to significantly decrease the thermal pressure of the Hugoniot state, with much of the  $P$ - $\rho$  regime between the Hugoniot and isentrope (or isotherm) being accessible with as little as 50 percent (1.5-fold) initial pre-compression (Fig. 5). Thus pre-compression is closely analogous to the application of multiple shocks, including in the fact that breaking a shock front into as few as 4 reverberations makes the compression nearly isentropic (22). As compressible fluids, such as  $H_2$  and  $He$  of planetary interest, can be subjected to relatively large pre-compressions, it is evident that the high-pressure thermodynamic state can be effectively tuned over a broad range of temperatures or internal energies (Fig. 6).

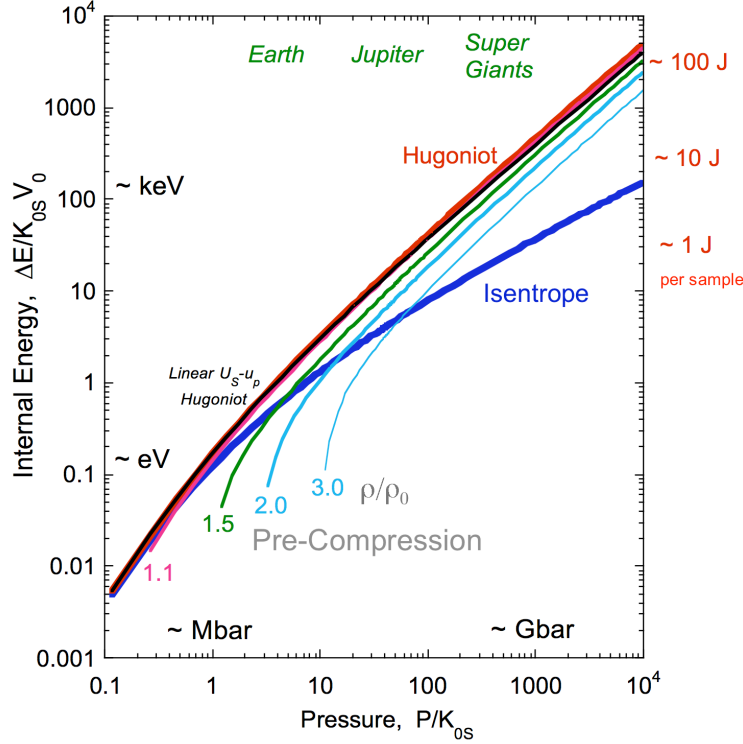


**Fig. 6.** Internal energy as a function of pressure corresponding to Fig. 5, showing the isentrope and the Hugoniots for initially uncompressed and pre-compressed samples. Approximate dimensional values for the axes are indicated assuming  $V_0 \sim 5$  cm per mol of atoms and  $K_{0s} = 10^{11}$  Pa; a typical pre-compressed sample size is about 400  $\mu$ m diameter by 10  $\mu$ m thick, or roughly 300 nmol of atoms. Note that the pressure dependence of the Hugoniot energy for the linear  $U_s - u_p$  relation (7) is similar to that derived from the Mie-Grüneisen analysis (9), even though the analogous pressure-density equations of state differ considerably (Fig. 5).

Megajoule-class lasers represent the state of the art in facilities currently under development for laser-shock experiments (23). As these consist of  $\sim 10^2$  beams, each delivering 1-10 kJ, Fig. 6 suggests that energies corresponding to Gbar pressures should be deliverable to a pre-compressed sample even if only a fraction of the beams can be used with limited efficiency (e.g., ten 1 kJ beams coupled at 1 percent efficiency to provide 100 J in the sample). As a result,

Gbar pressures relevant to large planetary interiors should become accessible in the laboratory for the first time.

One of the key benefits of the high energy-density laser facilities is not only that they deliver pulses having high power ( $\sim \text{PW}/\text{cm}^2$ ) over the 0.5-1 mm width of the sample area, but also that they can do so for the relatively long period of  $\sim 10\text{-}20$  ns (versus the  $\tau \sim 1\text{-}4$  ns effective pulse width of current facilities) (23). This is directly relevant to our experiments, because the shock front is followed by a rarefaction wave that develops at the end of the laser pulse (i.e., at time  $\tau$ ) and catches up with the shock in a time interval  $\Delta t$  from the initiation of shock loading. The shock-wave thus travels a distance  $U_S \Delta t$  before being attenuated. The rarefaction starts after the interface has traveled a distance  $u_p \tau$ , and travels at approximately the velocity  $U_S + u_p$  because the material is moving at velocity  $u_p$  and the local (high-pressure) sound velocity is about equal to the shock velocity. Therefore, the catch-up distance is

$$\Delta x = U_S \Delta t \approx (U_S + u_p)(\Delta t - \tau) + u_p \tau \quad (14)$$

such that

$$\Delta x \approx U_S^2 \tau / u_p \sim (10^2 \mu\text{m}/\text{ns}) \tau \quad (15)$$

As a result, a 10-20 ns pulse width allows use of a  $\sim 1\text{-}2$  mm thick diamond on the entry side, typical of the anvils that are used in static-compression experiments at Mbar pressures. Rather than being limited to the 1-10 GPa pressures, as at present, pre-compressions into the 100 GPa range should thus be possible in experiments at the largest laser facilities under development. That is, samples already transformed to a high-pressure (e.g., metallic) state could serve as starting materials for experiments to the 10-100 TPa level.

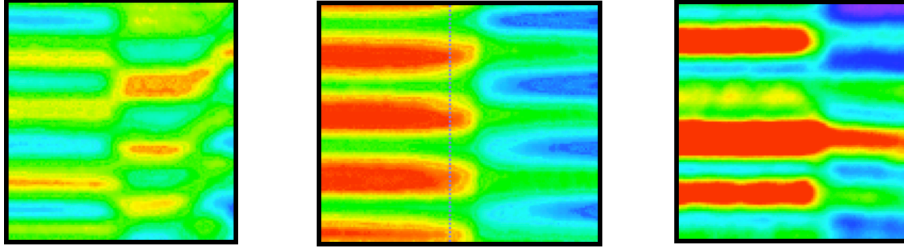


**Fig. 7.** VISAR records of shock-loaded  $\text{H}_2\text{O}$  (pre-compressed to  $\sim 1$  GPa) showing the transition from transparent behavior at  $P \sim 50$  GPa and  $T < 3500$  K (*left*: reflection of diamond-sample interface is visible through the shock-compressed sample); to opaque at  $P \sim 100$  GPa and  $3500 < T < 9000$  K (*center*); to reflecting at  $P > 150$  GPa and  $T > 9000$  K (*right*: reflection from shock front evident from time-dependent fringes) (14).

### Initial Experiments and Future Potential

Fig. 7 illustrates the potential of laser-shock experiments on pre-compressed materials. Here, VISAR is used to characterize the optical properties of the sample, as well as determining the Hugoniot pressure and density. In addition, an estimate of the blackbody temperature of the sample is obtained by optical pyrometry. The experiments clearly show that  $\text{H}_2\text{O}$  transforms from a transparent dielectric at low pressures and temperatures to a metallic-like state when

taken to pressures and temperatures exceeding 150 GPa and 9000 K (14). The profound change in outer, valence-electron states – chemical bonding – induced by high pressures and temperatures is visibly evident.

That pressure and temperature can be separately tuned is crucial, however, because either induces electronic changes in materials. Helium, for instance, can be either thermally ionized or pressure-ionized, and it is by varying the initial compression that one can experimentally validate theoretical expectations of the conditions under which the insulator–metal transition takes place (Fig. 8). The effect of ionization is to increase the density at a given pressure (or decrease the thermal pressure at a given density), which can be handled as a phase transformation and also through including a temperature dependence to the Grüneisen parameter. In fact, to the degree that electrons are thermally ionized, the thermal pressure becomes intrinsically a function of temperature and – along with other pressure-induced (e.g., structural) phase transitions – this softens the equation of state: higher densities are achieved for a given pressure.

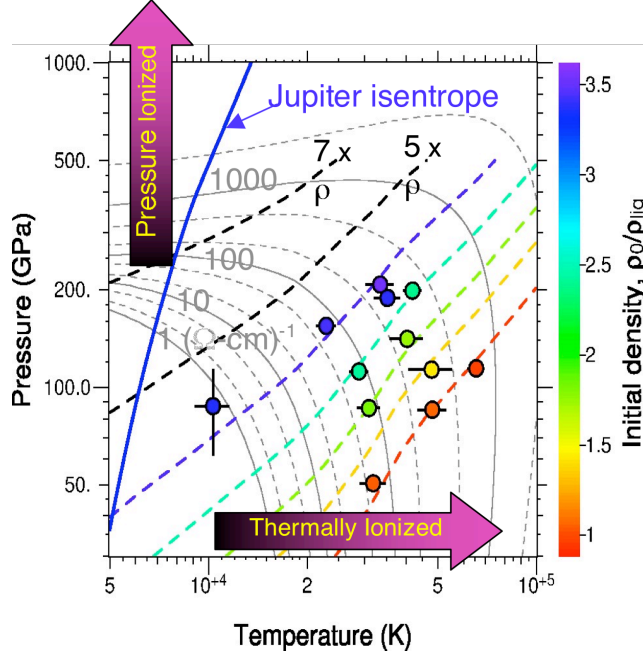


**Fig. 8.** Predicted contours of electrical conductivity (thin grey solid and dashed curves) for He as a function of pressure and temperature, showing that metallic properties can be induced either by high  $P$  or by high  $T$ . These influences can be separately documented by varying the initial density of the sample: dashed contours from lower left toward upper right, colored for low pre-compressions (1- to 3.5-fold initial compression) and black for 5- and 7-fold initial compression. Conditions at which several experiments have been performed are indicated by colored symbols, for which the electrical conductivity can be inferred from optical absorption and reflectivity (see Fig. 7). A model isentrope for Jupiter’s interior is shown for comparison.

These results illustrating dramatic changes in chemical bonding at Mbar (100 GPa) conditions reinforce the significance of being able to achieve significantly higher pressures in the

future (Fig. 6). Evidently, compressional-energy changes can reach keV in the Gbar (100 TPa) regime, comparable to energies of core-electron orbitals. Deep-electron levels within the atom can therefore participate in chemical bonding, and an entirely new type of chemistry becomes accessible in a (sub-nuclear) regime that is as yet unexplored by experiments.

1. Ragan, C. E., III (1982), *Phys. Rev. A* **25**, 3360-3375.
2. Trunin, R. F. (1998) *Shock Compression of Condensed Materials* (Cambridge Univ. Press, Cambridge, UK).
3. Cauble, R., Phillion, D. W., Hoover, T. A., Kilkenny, J. D. & Lee, R. W. (1993) *Phys. Rev. Lett.* **70**, 2102-2105.
4. Eremets, M. I. (1996) *High Pressure Experimental Methods* (Oxford Univ. Press, Oxford, U K).
5. Jeanloz, R. (1989) *Ann. Rev. Phys. Chem.* **40**, 237-259.
6. Hemley, R. J. & Ashcroft, N. W. (1998) *Physics Today* **51**, 26-32.
7. Butler, R. P., Wright, J. T., Marcy, G. W., Fischer, D. A., Vogt, S. S., Tinney, C. G., Jones, H. R. A., Carter, B. D., Johnson, J. A., McCarthy, C. & Penny, A. J. (2006) *Astrophys. J.* **646**, 505-522.
8. Zel'dovich, Y. B. & Raizer, Y. P. (2002) *Physics of Shock Waves and High-Temperature Hydrodynamic Phenomena* (Dover Publications, Mineola, NY).
9. Eliezer, S., Ghatak, A. & Hora, H. (2002) *Fundamentals of Equations of State* (World Scientific, Singapore).
10. Lee, K. K. M., Benedetti, L. R., Mackinnon, A., Hicks, D., Moon, S. J., Loubeyre, P., Occelli, F., Dewaele, A., Collins, G. W. & Jeanloz, R. (2002) in: *Shock Compression of Condensed Matter – 2001* edited by M. D. Furnish, N. N. Thadhani and Y. Horie (Am. Inst. Phys.), pp. 1363-1366.
11. Loubeyre, P., Celliers, P.M., Hicks, D. G., Henry, E., Dawaele, A., Pasley, J., Eggert, J., Koenig, M., Occelli, F., Lee, K.K. M., Jeanloz, R., Neely, D., Benuzzi-Mounaix, A., Bradley, D., Bastea, M., Moon, S. & Collins, G. W. (2004) *High-Pressure Research*, **24**, 25-31.
12. **Ruby fluorescence reference**
13. Marsh, S. P. (1980) *LASL Shock Hugoniot Data* (Univ. California Press, Berkeley, CA).
14. Lee, K. K. M., Benedetti, L. R., Jeanloz, R., Celliers, P. M., Eggert, J. H., Hicks, D. G., Moon, S. J., Mackinnon, A., Da Silva, L. B., Bradley, D. K., Unites, W., Collins, G. W., Henry, E., Koenig, M., Benuzzi-Mounaix, A., Paley, J. & Neely, D. (2006) *J. Chem. Phys.* **125**, 014701.
15. **VISAR reference**
16. McQueen, R. G., Marsh, S. P., Taylor, J. W., Fritz, J. N. & Carter, W. J. (1970) in *High Velocity Impact Phenomena* edited by R. Kinslow (Academic Press, San Diego, CA), pp. 294-419.
17. Jeanloz, R. (1989) *J. Geophys. Res.* **94**, 5873-5886.
18. Fabbro, R., Fournier, J., Ballard, P., Devaux, D. & Virmont, J. (1990) *J. Appl. Phys.* **68**, 775–784.
19. Lindl, J. D., Amendt, P., Berger, R. L., Glendinning, S. L., Glenzer, S. H., Haan, S. W., Kauffman, R. L., Landen, O. L. & Suter, L. J. (2004) *Phys. Plasmas* **11**, 339-491.
20. Holzapfel, G. A. (2000) *Nonlinear Solid Mechanics: A Continuum Approach for Engineering* (Wiley, New York, NY).
21. Birch, F. (1978) *J. Geophys. Res.* **83**, 1257-1268.
22. Lyzenga, G. A. & Ahrens, T. J. (1982) *Am. Inst. Physics Conference Proceedings* **78**, 231-235.
23. National Research Council (2003) *Frontiers in High Energy Density Physics* (National Academies Press, Washington, DC).